

“Minimalist” Nanovaccine Constituted from Near Whole Antigen for Cancer Immunotherapy

Kun Wang,^{†,‡,#} Shuman Wen,^{†,‡,#} Lianghua He,[†] Ang Li,^{||} Yan Li,[†] Haiqing Dong,[†] Wei Li,[⊥] Tianbin Ren,[‡] Donglu Shi,[§] and Yongyong Li^{*,†,⊥}

[†]Shanghai East Hospital, The Institute for Biomedical Engineering & Nano Science, Tongji University School of Medicine, Shanghai 200092, PR China

[‡]School of Materials Science and Engineering, Tongji University, 4800 Caoan Road, Shanghai 201804, PR China

[§]The Materials Science & Engineering Program, Department of Mechanical & Materials Engineering, College of Engineering & Applied Science, University of Cincinnati, Cincinnati, Ohio 45221, United States

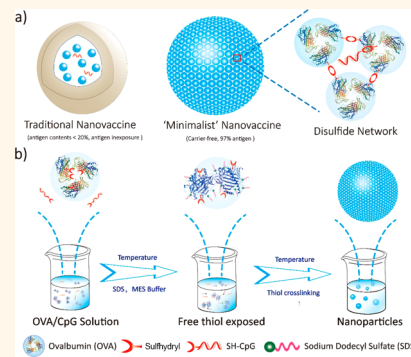
^{||}School of Life Science and Technology, Tongji University, 1239 Siping Road, Shanghai 200092, PR China

[⊥]International Joint Cancer Institute, The Second Military Medical University, Shanghai 200433, PR China

Supporting Information

ABSTRACT: One of the major challenges in vaccine design has been the over dependence on incorporation of abundant adjuvants, which in fact is in violation of the “minimalist” principle. In the present study, a compact nanovaccine derived from a near whole antigen (up to 97 wt %) was developed. The nanovaccine structure was stabilized by free cysteines within each antigen (ovalbumin, OVA), which were temporally exposed and heat-driven to form an extensive intermolecular disulfide network. This process enables the engineering of a nanovaccine upon integration of the danger signal (CpG-SH) into the network during the synthetic process. The 50 nm-sized nanovaccine was developed comprising approximately 500 antigen molecules per nanoparticle. The nanovaccine prophylactically protected 70% of mice from tumorigenesis (0% for the control group) in murine B16-OVA melanoma. Significant tumor inhibition was achieved by strongly nanovaccine-induced cytotoxic T lymphocytes. This strategy can be adapted for the future design of vaccine for a minimalist composition in clinical settings.

KEYWORDS: minimalist nanovaccine, ovalbumin, disulfide network, nanoassembly, cancer immunoprotection



Vaccines, developed to provoke the immune response, have been recognized as the most effective medical intervention for human public health.¹ Research has long been focused on developing vaccines with “minimalist” compositions intended to reduce biological risks accompanied by the “isolate–inactivate–inject” paradigm.² To this end, antigens (typically proteins), screened and extracted from pathogens, are used to pulse the immune system for health protection or disease treatment. However, these “purified” antigens suffer from low immunogenicity in the activation of sufficient immune responses.³ Adjuvants have thus been employed as an antigen reservoir (depot effect) to boost antigen immunogenicity.⁴ The most intriguing example is the clinical use of aluminum salt adjuvants in vaccines for the past 90 years.⁵ However, the limited capacity to elicit T cell responses has been the major obstacle for antitumor vaccines.^{6,7} Several adjuvants have been recently developed

and licensed for vaccine development,⁴ showing promise for cancer immunotherapy.^{7,8}

Synthesized or bioderived nanocarriers have been extensively investigated, as promising adjuvants, capable of packaging antigens at the nanoscale^{9–14} (such as polymeric¹⁰ or virus-like¹⁵ particles). Similar to conventional adjuvants, these nanocarriers exhibit considerable depot effects for persistent activation of antigen presenting cells (APCs).¹³ Furthermore, these nanocarriers mimic pathogens, such as viruses,⁸ for antigen cross-presentation.^{1,16} This advantage largely relies upon the capacity for cytosol delivery to simulate T cell response, a key step for antitumor effect. Systemic transportation can also be achieved through diffusion into lymph nodes (LNs) to spatially expand antigen presentation *in situ* to

Received: January 22, 2018

Accepted: June 21, 2018

Published: June 21, 2018

distant lymph tissue.^{17,18} Other versatile nanocarrier functions (imaging,¹⁹ targeting,²⁰ and intracellular delivery^{21,22}) can further enhance antitumor efficacy to meet additional requirements in clinical settings.^{23,24}

One of the major challenges in nanovaccine design has been the tendency to incorporate overly abundant adjuvants (such as liposomes¹¹ or poly(lactic-co-glycolic acid) (PLGA)²⁵), a violation of the minimalist principle.²⁶ Another issue deals with the difficulty in achieving virus-like multicopy display as a result of antigen entrapment impeding antigen exposure. Surface multicopy display is harnessed by viruses to mediate a potent immune response.¹ Additionally, some nanocarriers generate unexpected immune responses that considerably compromise therapeutic outcomes. In particular, poly(ethylene glycol) (PEG), the most common polymer nanocarrier, has been identified as “immunogenic”.²⁷ The PEG antibody generated can lead to rapid clearance of PEG-based drugs or vaccine delivery systems from body.²⁸

In this study, we designed a nanovaccine with minimalist immune compositions while maintaining adjuvant properties of conventional nanovaccine. The approach is to self-assemble protein antigens (OVA) by exposing free thiols embedded in hydrophobic regions followed by the formation of an intermolecular disulfide network at the nanoscale for structural fixation (Figure 1). In this fashion, a nanovaccine is constituted with superhigh antigen packaging (97%) and the necessary CpG agonist (3%), without the assistance of any exterior

nanocarriers. The construction nearly entirely from antigen is not only consistent with the principle of minimalist composition but also with an extremely high antigen density, highly preferred for APC interactions. Advantages of antigen and CpG coordination include enhanced “antigen depot”, dendritic cell (DC) maturation, LN transportation, and elicitation of endogenous T cell responses. These biostructural characteristics are fundamentally important in preventing tumorigenesis and are experimentally demonstrated by application of B16-OVA melanoma model in C57BL/6 mice.

RESULTS

Design Strategy. OVA as a classic model antigen²⁹ is frequently co-delivered with CpG agonist (which activates TLR9 ligand as a danger signal to initiate immune responses³⁰) via various nanocarriers.^{2,31,32,33} For OVA antigen, four free thiols in each OVA molecule³⁴ can theoretically ensure sufficient intermolecular cross-linking to form a network at the nanoscale. Incorporation of a terminal thiol group enables CpG to be integrated into the disulfide network. The cleavable disulfide bonds upon intracellular reduction³⁵ facilitates the selective release of CpG inside DCs where TLR9 is located.³⁶

As free thiol groups are typically embedded within the OVA hydrophobic region,³⁷ they are not readily accessible for intermolecular cross-linking. Moderate protein denaturation is therefore needed to liberate the free thiols,³⁸ which are supposed to form the intermolecular disulfide network in stabilizing the OVA@CpG nanoassembly. The biostructural design is able, without any other carriers, to protect OVA antigens and CpG oligonucleotides (short half-life *in vivo*) from rapid degradation and clearance *in vivo* for intense immune activation.

Synthesis, Physicochemical Properties, and Formation Mechanism of OVA@CpG Nanoparticles.

As an initial attempt, we first sought to find out if there exists a critical temperature that enables nanoassembly formation via an intermolecular disulfide network. OVA in MES buffer was therefore heated under different temperatures. At 70 °C, the reaction solution gradually became slightly opalescent during the reaction. The size of resultant nanoparticles could be controlled from 30 to 400 nm depending on the reaction time. Circular dichroism (CD) revealed OVA protein unfolding after the heating process (Figure S1). However, the nanoparticle was not disulfide-fixed but noncovalently assembled instead. This is supported by the fact that treatment with urea or SDS led to rapid nanoparticle disassembly, as shown by dynamic light scattering (DLS) assay (Figure S2). This result suggests inadequate formation of the disulfide bond network.

With an optimized pH and temperature, we found that a small amount of SDS incorporation led to OVA nanoparticles with the desired “disulfide-fixed” stability, although the assembly process required a prolonged reaction time. Reduction of the sulfhydryl concentration of OVA protein after nanoparticle formation suggested disulfide formation (Figure 2a). OVA@CpG nanoparticles were developed by incorporating thiol-terminated CpG (CpG-SH). Mechanistic analysis revealed a definite, decisive role of disulfide bond in OVA@CpG assembly. Even with SDS treatment, the size of the OVA@CpG assembly remained constant during 48 h of monitoring, with only minor increase due to swelling. However, following treatment with dithiothreitol (DTT, a regular agent to cleave disulfide), a rapid nanoparticle destruction was shown by size change, particularly at higher

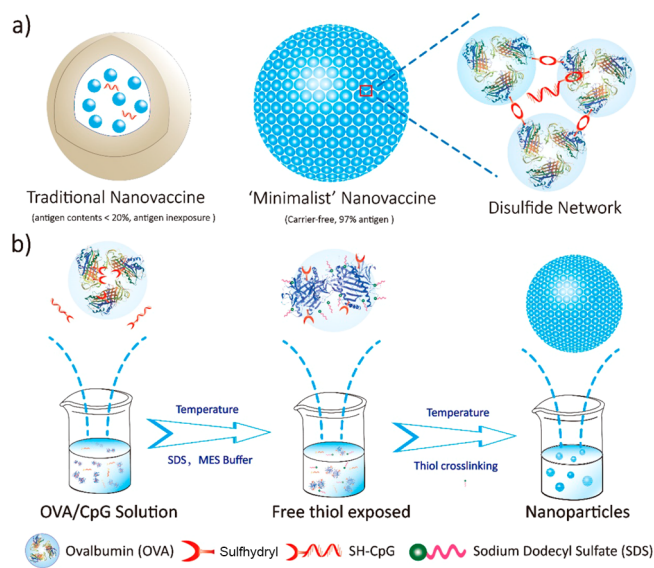


Figure 1. Scheme for the structure and assembly of OVA@CpG nanoparticles with 100% immune compositions: (a, left) traditional nanovaccine, with low antigen loading efficiency (generally <20%) and difficult antigen exposure due to entrapment by carriers, such as poly(lactic-co-glycolic acid) (PLGA) nanospheres; (a, right) hypothesized structure of OVA@CpG nanoparticles assembled from a near whole antigen supplemented with minimal CpG agonist, fixed through a disulfide network. (b) Schematic diagram of the assembly procedure. Thiol groups in OVA structure are exposed under treatment with a hydrophobic regulator (sodium dodecyl sulfate, SDS) and subsequently are heat-driven to form OVA@CpG nanoparticles through disulfide bonds. The as-developed strategy for the nanoengineering of OVA and CpG uses green-synthetic techniques and is straightforward and highly size-controlled.

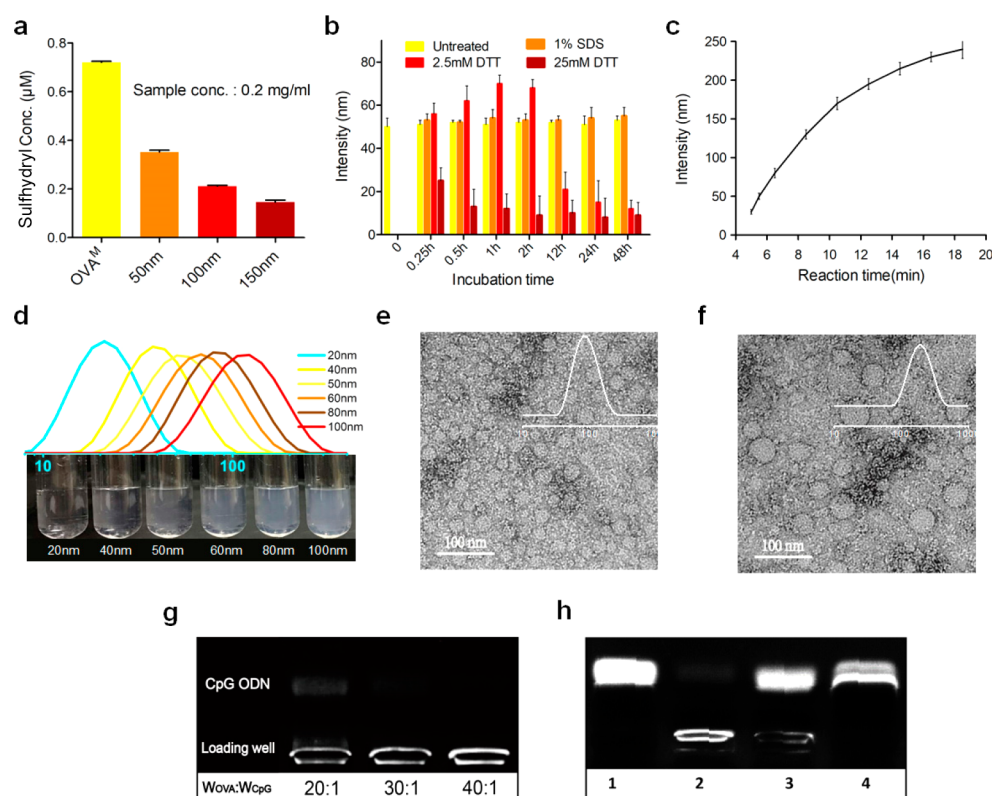


Figure 2. Characterization of the physicochemical properties. (a) Sulfhydryl concentration of molecular OVA and OVA particles at 50, 100, and 150 nm. (b) Size stability of OVA@CpG nanoparticles after treating with excess SDS and DTT. (c) Growth of the OVA@CpG nanoparticle size over the reaction time, showing precision in size regulation. Data are presented as mean \pm SD ($n = 3$). (d) Photographs of the OVA@CpG nanoparticle solutions (1.5 mg mL^{-1}) with their respective size distribution. (e, f) TEM analysis and size distribution of two representative OVA@CpG nanoparticles. (g) Gel electrophoresis to show the capacity of OVA to carry CpG during assembly. OVA and CpG were assembled with weight ratios of 20:1, 30:1, or 40:1 (OVA/CpG). (h) Gel electrophoresis to show the resistance to DNase I degradation and selective reduction-triggered release of CpG. Molecular CpG without treatment (lane 1); OVA@CpG nanoparticles (OVA_{wt}/CpG_{wt} = 30:1) treated with DNase I (lane 2); OVA@CpG treated with DNase I, followed by heat-deactivation of the enzyme, and finally treatment with DTT (lane 3); OVA@CpG treated with DNase I, followed by heat-deactivation of the enzyme, and finally treatment with DTT + SDS (lane 4).

DTT concentration or lower particle size (Figure 2b and Figure S3). Additionally, the nanoparticles displayed considerable biostability when cultured in complete RPMI medium or PBS (Figure S3). The UV spectrum of OVA@CpG nanoparticles (Figure S4) was slightly blue shifted compared with the mixture of molecular OVA and CpG (OVA^M&CpG^M). This alteration is probably associated with the partial unfolding of protein structure.

The size of the OVA@CpG nanoparticle was precisely controlled from tens to hundreds of nanometers (Figure 2c), depending on the reaction time. The nanoparticle solutions gradually became opalescent as the particle size increased, with a narrow size distribution (Figure 2d).

Transmission electron microscopy (TEM) images of representative samples (hydrodynamic size, 70 nm and 150 nm) showed well-dispersed, regular spherical nanoparticles (Figure 2e,f). The spherical shape was confirmed by the index of scattering particle topology (ρ value close to 1) (Figure S5). It is estimated that approximately 500 antigen molecules were assembled to form one 50 nm nanoparticle, as characterized by dynamic laser light scattering (LLS) (Figure S5). The effective encapsulation of CpG into nanoparticles was confirmed by gel electrophoresis (Figure 2g) and UV spectral analysis (Figure S4). The CpG migration in agarose gel was completely retarded for the OVA@CpG nanoparticles at the weight ratios

(OVA_{wt}/CpG_{wt}) of 30:1 or 40:1, suggesting efficient CpG condensation. The feed ratio of OVA to CpG was chosen to be 30:1 in the following study. CpG-loaded nanoparticles displayed considerable protection against DNase I degradation; however, CpG was released when assemblies were treated with DTT, showing binding of OVA and CpG through disulfide bonds (Figure 2h and Figure S6). SDS-PAGE analysis showed no noticeable free OVA band, indicating negligible OVA protein left in the nanoparticle synthesis (Figure S6).

OVA@CpG Nanoparticle Promoted Cellular Uptake and Activated APCs *in Vitro*. Antigen uptake and APCs (macrophage and DC) activation are key steps in the generation of potent immune responses.^{39,40} We first identified phagocytized efficiency of OVA@CpG nanoparticles (hereafter denoted as mNV) by bone marrow-derived DC (BMDC) and DC2.4 as a function of incubation time (Figure 3a,b). The mNV concentration was chosen according to cytotoxicity assay (Figure S7). Fluorescent mNVs containing FAM-labeled CpG (mNV^F) and mNVs containing BODIPY-labeled OVA (mNV^B) were used for detection, with FAM-labeled CpG (CpG^F) and BODIPY-labeled OVA (OVA^B) as the controls, respectively. Quantitative fluorescence analysis showed enhanced CpG internalization of mNVs in contrast to molecular CpG. Additionally, OVA uptake was also significantly increased at 12 and 24 h incubation time points in DC2.4

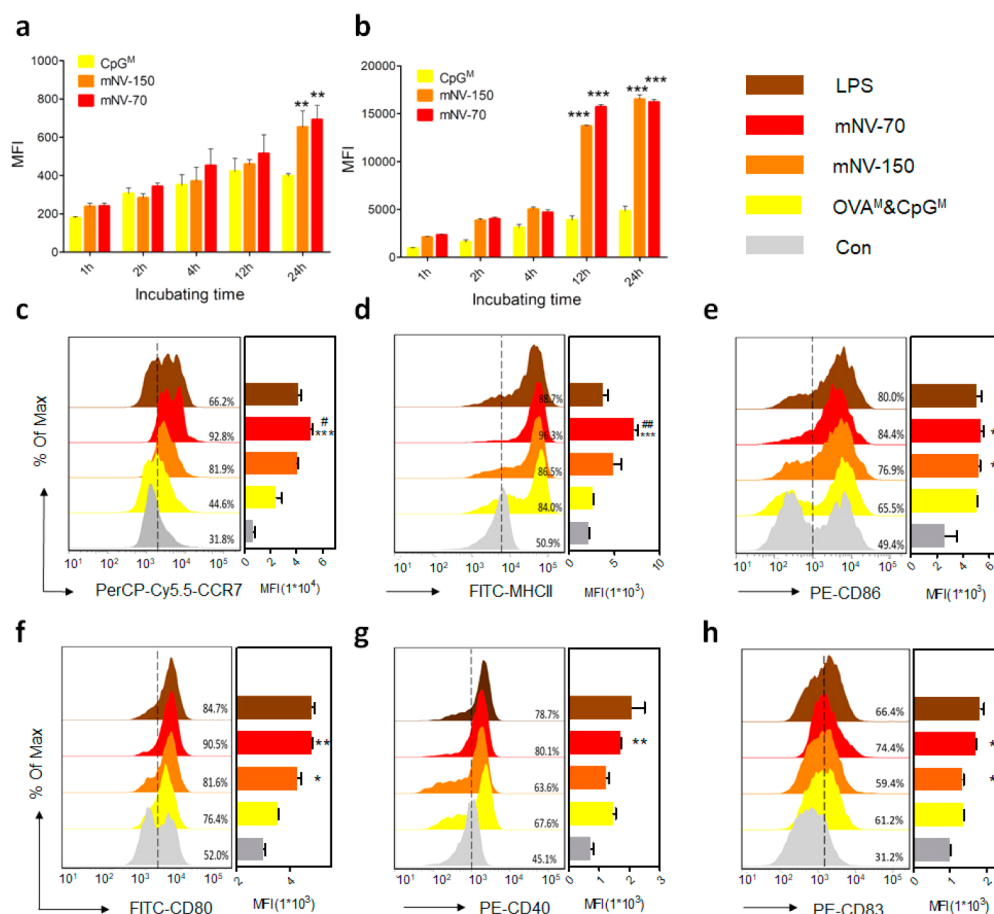


Figure 3. DC cellular uptake and maturation induced by mNVs. mNV uptake by (a) BMDC and (b) DC2.4 incubated for 1, 2, 4, 12, and 24 h, with CpG as the control. BMDC maturation was quantitatively detected using flow cytometry, with medium as the negative control and LPS as the positive control. Individual histograms are shown for (c) CCR7, (d) MHCII, (e) CD86, (f) CD80, (g) CD40, and (h) CD83. Data are presented as mean \pm SD ($n = 3$). * $p < 0.05$, ** $p < 0.01$ and *** $p < 0.001$ vs untreated cells. # $p < 0.05$ and ## $p < 0.01$ vs cells treated with the molecular group.

(Figure S8). Potentiated endocytosis for both CpG and OVA indicated a co-delivery synergy. The internalization process was visibly observed using confocal microscopy (Figure S9). BMDCs after 24 h stimulation expressed higher levels of TNF- α and IL-6, suggestive of potential cellular immunity (Figure S10).

The maturation of BMDCs was investigated after mNV stimulation for 24 h, with lipopolysaccharides (LPS) as the positive control. The characteristic markers of CD40, CD80, CD86, CD83, CCR7, and MHC II were analyzed using flow cytometry and quantified with the mean fluorescence intensity (MFI). The 70 nm particles (mNV-70) greatly elevated the expression levels of CCR7 (92.8%), MHC II (96.3%), CD80 (90.5%), and CD86 (84.4%), even higher than stimulation with LPS (CCR7, 66.2%; MHC II, 88.7%; CD80, 84.7%; CD86, 80.0%). Though not as efficient as mNV-70, incubation with mNV-150 (the 150 nm particles) showed comparable marker upregulation to that with LPS. CCR7, the most prominent among all characteristic markers, suggests enhanced migration capacity.⁴¹ Additionally, OVA nanoparticles without CpG exhibited a self-adjunct property similar to the PLGA nanoparticles (Figure S11).

mNV Promoted Retention in Injection Site and Draining LNs. To investigate the transportation and retention properties of mNVs, C57BL/6 mice were subcutaneously injected in the inguinal region with mNV^B, OVA^B, mNV^F, and

CpG^F, respectively. As shown in Figure 4a, fluorescence was undetectable at the injection sites after 96 h for the OVA molecule, while the mNV-treated group showed a prolonged signal even after 168 h. The signal of naked CpG rapidly degraded (within 12 h) and was nearly invisible for *in vivo* detection (Figure 4d). In contrast, mNVs prevented CpG from rapid decomposition for as long as 96 h with persistent fluorescence, indicating a considerable co-delivery synergy.

Images of isolated draining LNs (Figure 4b–f) showed that mNVs rapidly accumulated within LNs at 4 h and persisted over 168 h for mNV^B (96 h for mNV^F). For quantitative analysis, the cells isolated from LNs were examined using flow cytometry (Figure 4c,f). It was found that 16.3% of the positive (fluorescence⁺) lymphocyte cells in the mNV^B group exhibited detectable fluorescence for 168 h, while 13.0% of the cells in the mNV^F group exhibited fluorescence for 96 h. The values were 10-fold higher than the molecule-treated group. The above results indicated that mNVs favored both depot effect and LN migration.

mNV Elicited a Potent Antitumor Immune Response *in Vivo*. As a potential therapeutic nanovaccine, the antitumor performance of the mNVs was assessed. B16-OVA cells (5×10^4) were subcutaneously injected into the right flank of mice followed by three immunizations at intervals of 4 days.⁴² In contrast to the groups of saline or OVA^M&CpG^M, the tumors in mNV groups grew much slower (Figure 5a and Figure S12).

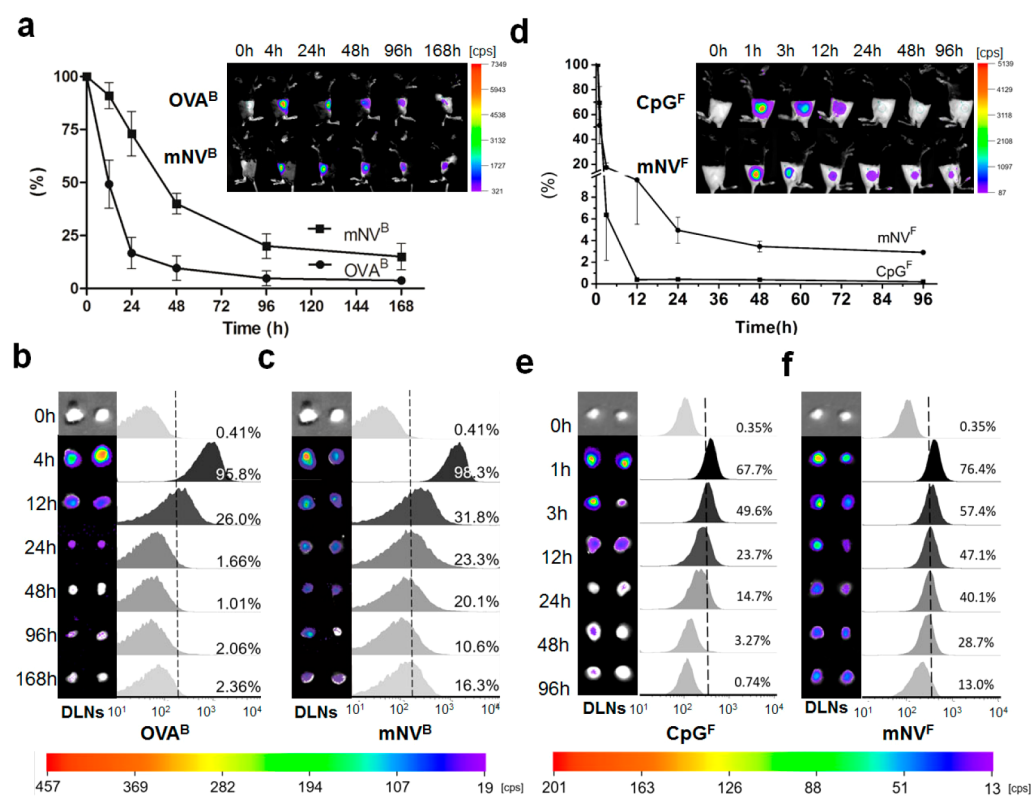


Figure 4. mNV-70 depot at the injection site and transport into draining LNs investigated using an *in vivo* imaging system. C57BL/6 mice were subcutaneously injected in the inguinal region with mNV^B, OVA^B, mNV^F, or CpG^F. Antigen fluorescence at injection sites was evaluated and documented (a) at 0, 4, 24, 48, 96, and 168 h for mNV^B or OVA^B and (d) at 0, 1, 3, 12, 24, 48, and 96 h for mNV^F or CpG^F. Data are presented as mean \pm SD ($n = 3$). The representative fluorescence images of the draining LNs (DLNs) for groups of (b) OVA^B, (c) mNV^B, (e) CpG^F, and (f) mNV^F at the indicated time points. The cells were collected from the isolated DLNs to quantitatively analyze time dependent LN accumulation of antigen and CpG using flow cytometry.

The group immunized with mNV-70 displayed significantly retarded tumor growth (Figure 5a), compared with the group receiving mNV-150, showing the critical role of size. mNV-70 facilitated a prolonged mean survival time of more than 28 days, which was accompanied by a significantly improved survival rate (Figure 5b). To examine the antitumor immunization for a larger dose of tumor cells, 10-fold higher population of B16-OVA cells (5×10^5) was applied using the same experimental schedule. Despite gradual tumor growth, the survival rate (Figure 5c) of mNV-70 (100%) or mNV-150 (60%) groups remained much higher than that of the control group, which experienced continuous tumor growth with a mean survival time of less than 15 days.

mNV Induced Tumor Prevention. To investigate the prophylactic efficacy of mNVs against B16-OVA melanoma, C57BL/6 mice were immunized three times at one-week intervals, with complete Freund's adjuvant (FA) supplemented with OVA as a positive control. B16-OVA cells (5×10^4) were subcutaneously injected in the right flank of mice 1 week after the last immunization. The percentage of mice with no detectable tumor masses (Figure 5d,e) during the investigated period reached 70% for mNV-70 immunization but only 30% for mNV-150 immunization ($n = 10$). The tumor-free mice in the mNV-70 group remained tumor-free up to 18 weeks. Moreover, tumor growth was significantly delayed in those mice in which tumor occurred compared with the positive control group (Figure 5d). However, mice immunized with OVA^M&CpG^M succumbed to a steady tumor growth with marginal survival benefits (Figure S12). Importantly, no

significant fluctuation of body weight was observed (Figure S13), indicating insignificant toxicity in animals immunized multiple times with mNVs. The survival ratio (Figure 5f) reflected the potent inhibitory effect of tumors elicited by mNV-70 (100% survived during the investigated period).

Mechanistic Study. We next investigated the underlying mechanism for the antitumor effect elicited by mNVs. The serum levels of TNF- α and IL-12 (p40) were significantly increased in mice treated with mNVs (Figure 6a,b). These cytokines represent important indices for successful induction of antitumor immune responses. The single-cell suspensions of draining LNs, spleen, tumor, and peripheral blood were acquired according to the reported protocol.^{43–45} The expression levels of the costimulatory molecules (CD80, CD86, and CD40) and MHC II in isolated CD11c⁺ DCs from the draining LNs were analyzed by flow cytometry. The results showed a significant shift from the immature to the mature phenotype in the prophylactic (Figure 6c–f) and therapeutic groups (Figure S14). The CD80⁺ expression level of cells in the mNV-70 treated group exhibited 31.6% upregulation, which was in sharp contrast to the controls (<14%), as well as mNV-150 group (<20%). This result is consistent with the BMDC maturation triggered through mNVs *in vitro*.

The CD8/CD4 T cell ratio in the CD3⁺ lymphocyte subset is a significant indicator of the outcome of adaptive T cell immunotherapy,⁴⁶ where a decreased CD8/CD4 ratio is generally associated with a negative outcome. In the prophylactic test, the ratio observed in the mNV-70 group

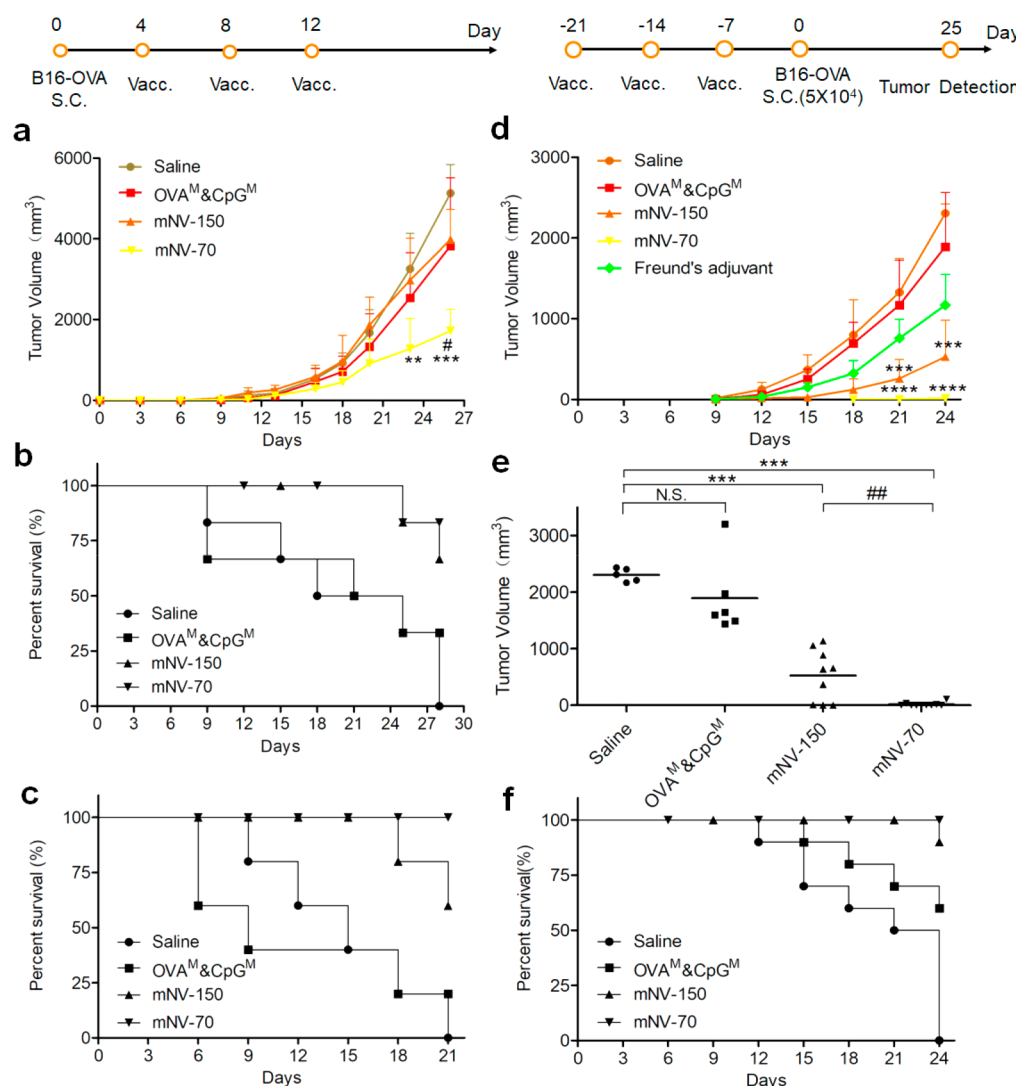


Figure 5. mNV-induced prophylactic and therapeutic immune effects in the B16-OVA model. For therapeutic experiment, C57BL/6 mice were subcutaneously inoculated with 5×10^4 B16-OVA tumor cells and vaccinated with the indicated formulations on days 4, 8, and 12. (a) Average tumor growth curves and (b) survival rates are shown ($n = 6$). (c) The survival rate of the mice subject to the challenge of 10 -fold population of B16-OVA cells (5×10^5) under the same vaccination protocol. For prophylactic experiment, mice were subcutaneously inoculated with 5×10^4 B16-OVA tumor cells after being prevaccinated with the indicated formulations three times at one-week intervals. (d) Average tumor growth curves, (e) tumor volume on day 25, and (f) survival rates are shown ($n = 10$). Data are presented as mean \pm SD, $**p < 0.01$ and $***p < 0.001$ vs the saline group, $\#p < 0.05$ and $\#\#p < 0.01$ vs the mNV-150 group, NS indicates $p > 0.05$.

was significantly higher than that of control group ($p < 0.001$) (Figure 7a,b). A similar tendency was also observed in the immunotherapy test (Figure 7c,d), suggesting a stronger upregulation of splenic CD8⁺ T lymphocyte subset induced by mNV-70. To investigate OVA specificity of the generated cytotoxic T lymphocytes (CTLs), splenocytes stained with carboxyfluorescein succinimidyl ester (CFSE) were restimulated by antigen *in vitro* and monitored for CTL proliferation. Upon each division, cells will generally lose half of their CFSE label. Fluorescent intensity of CD8⁺ T cells from the mNV-70 group reduced dramatically compared with the control group. A ratio of 33:1 fluorescence intensity of mNV-70 versus control group showed an average >5-fold multiplication (5 generations), higher than mNV-150 group (4 generations) and molecule group (2 generations), as shown in Figure 7e,f.

Subsequently, OVA-specific CTL killing capacity was measured using cytotoxicity detection kit with lactate dehydrogenase (LDH). After 168 h restimulation by antigen

in vitro, mNV-70 group generated considerable cytotoxic effect (40%) against B16-OVA cells even at effector-to-target ratio of 10:1, 2-fold increase over mNV-150 group (Figure 7g). These results reveal that mNV-70 can more efficiently stimulate the generation of OVA-specific CTLs. Additionally, spleen T cells from mice immunized with mNV-70 or mNV-150 upon stimulation with OVA produced significant amounts of IFN- γ (521 and 307 pg mL⁻¹, respectively) (Figure 7h). Expressions of elevated IFN- γ with stable IL-4 (Figure 7i) suggested that mNVs induced a biased Th1-type immune response, which is favorable for antitumor effect.⁴⁷

The tetramer assay of OVA-specific CD8⁺ T cells in peripheral blood and spleen was subsequently examined on day 14. The frequency of OVA-specific CD3⁺CD8⁺tetramer⁺ T cells were quantitatively detected by flow cytometry. In spleen, mNV-70 elicited 2.52% OVA-specific CD8⁺ T cells, markedly higher than the other groups (Figure 8a,b). In peripheral blood, mNV-70 elicited a peak frequency of 23.7% OVA-

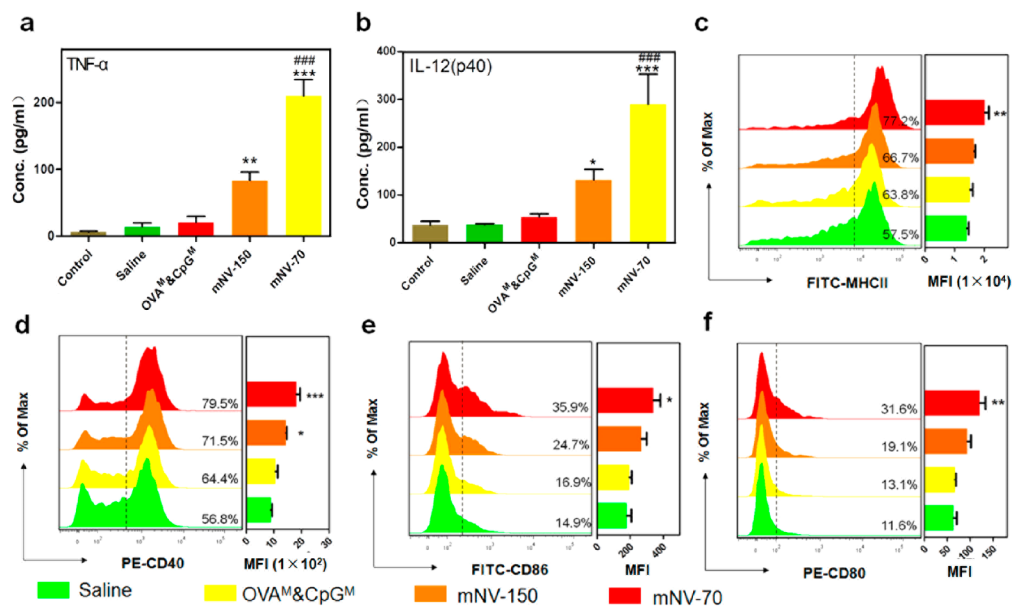


Figure 6. mNVs inducing DC maturation of draining LNs in prophylactic experiment. The serum levels of (a) TNF- α and (b) IL-12 (p40) from mice on day 14 were measured using ELISA. The cells from the isolated LNs of immunized mice were stained with (c) FITC-MHCII, (d) PE-CD40, (e) FITC-CD86, and (f) PE-CD80 antibodies to characterize the maturation of DCs *in vivo*. Data are presented as mean \pm SD ($n = 4$). * $p < 0.05$, ** $p < 0.01$, and *** $p < 0.001$ vs the control group; # $p < 0.05$ and ## $p < 0.01$ vs the mNV-150 group.

specific CD8⁺ T cells (Figure 8c,d). Of note, one can conclude that the priming efficiency is highly associated with particle size, with 3–5-fold increase when size is reduced from 150 to 70 nm. OVA-specific IFN- γ production in splenocytes was also efficiently induced by mNV (Figure S15) using ELISPOT. The tetramer assay results for OVA-specific CD8⁺ T cells in therapeutic protocol are shown in Figure S16. These results demonstrated that mNVs can significantly augment OVA-specific CTLs with killing capacity of target melanoma cells.

To further validate the infiltration of CTLs in tumors, cryostat sections of the tumors from prophylactically treated mice were stained with anti-CD8 antibody (green) (Figure 8e). The results showed a large number of CD8⁺ T cells (green signal) infiltrating and accumulating in the tumors of mNV-immunized mice. The ratio of CD3⁺CD4⁺ or CD3⁺CD8⁺ T cell infiltration within tumors was quantitatively characterized by flow cytometry (Figure 8f,g). Increased CTL distribution (5–8-fold) was observed in tumor tissues from mNV immunized mice as compared to the control groups. The CTL infiltration in the therapeutic test conditions is shown in Figure S17.

DISCUSSION

The principle of minimalist composition has shown great success in prophylactic vaccine development, in close association to the discovery of adjuvants (like aluminum adjuvants). It has remained a challenge to replicate the same success for tumor vaccines. The underlying mechanism is largely associated with the inability of conventional adjuvants to elicit sufficient T cell immune response. Nanovaccinology has shed light on the above critical issue by densely packaging antigens in a single nanoparticle, somewhat analogous to the particulate microbes. However, conventional nanovaccines have to use additional nanocarriers for the required formulation.

To address this critical challenge, we have developed an “antigen carries antigen” strategy by forming an intermolecular

disulfide network between antigens, through which mNVs with precision size can be yielded. The key underlying principle is to expose free cysteines by partial denaturation while avoiding fast hydrophobic aggregation with SDS. CpG (3 wt %) terminated with thiol groups can be further incorporated through integration into the disulfide network as a “danger signal” to activate DCs (known as the most efficient APCs). The resultant mNVs were assembled from a near whole antigen, characterized by high-density antigen packaging. They were biostructurally stable in serum and capable of protecting fragile CpG within mNVs from DNase I degradation.

As the most efficient APCs, DCs play an important role in the recognition and collection of antigen information to initiate specific immunity. mNVs feature a minimalist composition, being engineered from a near whole antigen (up to 97 wt %). This “antigen carries antigen” strategy avoids the necessity of antigen encapsulation into conventional nanocarriers, which is not favorable for antigen exposure. The biological skeleton is similar to viruses or bacteria for antigen display, different from soluble proteins. mNVs are found to exhibit a gradual, time-dependent, and intracellular accumulation of CpG, more prominent than their molecular counterparts, showing the synergistic co-delivery of OVA and CpG. Expectedly, mNVs significantly promote DC maturation and boost antigen presentation efficiency after uptake. The APC stimulation is at least comparable to that with known adjuvants, such as PLGA and LPS.

The efficiency of synergistic co-delivery is further supported by the local depot effect at the immunized sites and transportation to LNs. Upon subcutaneous immunization, both molecular CpG and OVA show rapid clearance to an insignificant level at 24 h within LNs, reflecting biological instability. However, mNVs comprising only molecular OVA and CpG display considerable accumulation in LNs and retarded release at the injection sites, which is favorable for generation of immune responses.

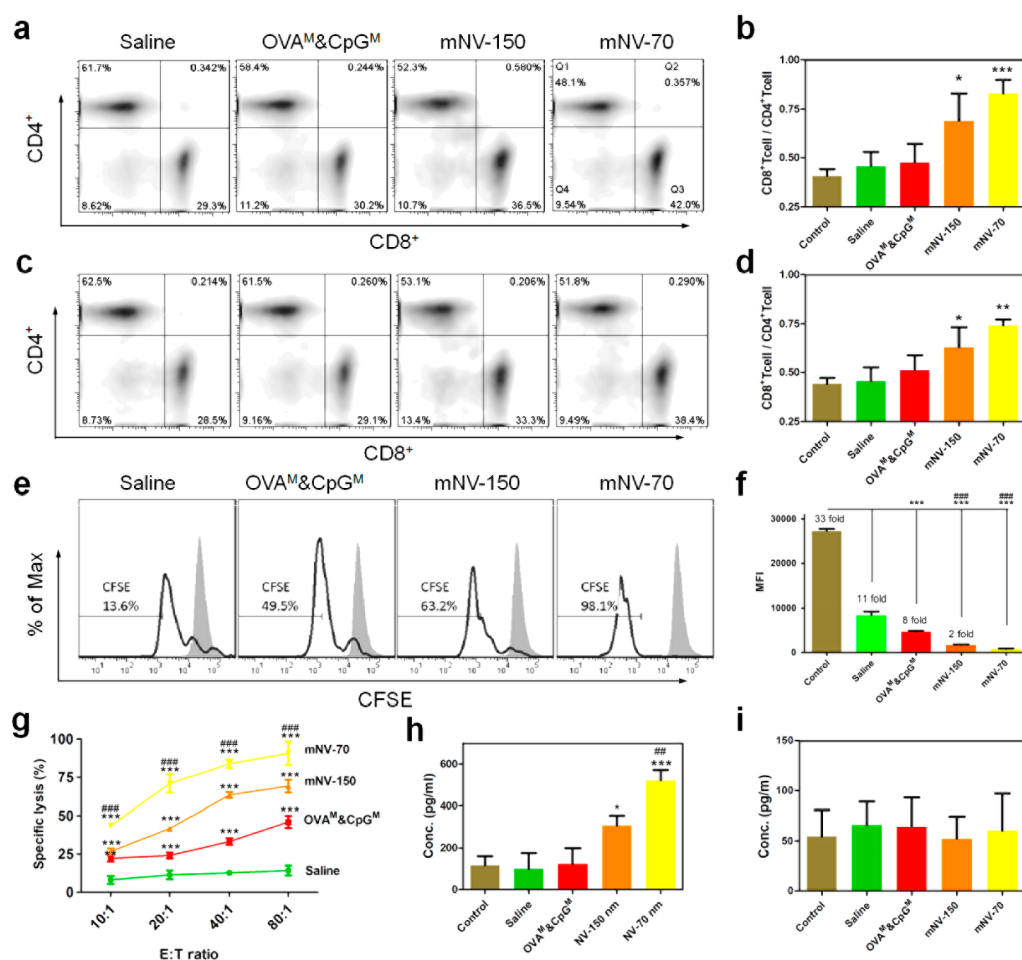


Figure 7. Stimulation and specificity of T cell responses. To validate the CTL effect generated from mNVs, mice were sacrificed on day 14 for prophylactic test and on day 24 for therapeutic test. The proportion of CD3⁺CD4⁺ and CD3⁺CD8⁺ T cells in splenocytes from mice in (a, b) prophylactic and (c, d) therapeutic experiments is quantified. The CFSE labeled splenocytes from prophylactic mice were restimulated by OVA antigen *in vitro* to assess the proliferation of antigen specific CTLs. (e, f) After 48 h incubation, the proliferation of CD8⁺ T cells was assessed by CFSE dilution, with unstimulated CD8⁺ T cells as the control (gray shade). (g) After additional 7 days restimulation, LDH release tests were performed by taking cultured splenocytes as effector cells. Splenocytes were cocultured with B16-OVA cells (target cell) at different E/T ratios 10:1, 20:1, 40:1, or 80:1 for 6 h. Amount of (h) IFN- γ and (i) IL-4 in splenocyte supernatant after 48 h restimulation with OVA antigen, measured by ELISA. Data are presented as mean \pm SD ($n = 4$). * $p < 0.05$, ** $p < 0.01$ and *** $p < 0.001$ vs the saline group; #### $p < 0.001$ vs the OVA^M&CpG^M group.

Subsequently, the results from B16-OVA murine melanoma models verify the antitumor prophylactic and therapeutic efficiency of mNVs. In the prophylactic experiments, mice immunized with mNV-70 show markedly inhibited tumorigenesis, with 70% of the mice (7 in 10) remaining tumor-free for the entire investigation period. In sharp contrast, no tumor-free mice are observed for the positive control group (complete FA combined with OVA) but with delayed tumorigenesis compared to the negative control. In the therapeutic test, the tumor growth is effectively delayed in mNV-treated mice resulting in prolonged mean survival time.

Analysis of draining LNs revealed a higher level of DC maturation, which has conditioned the subsequent cascade of immune responses. Cytokine secretion from splenic lymphocytes (elevated IFN- γ with stable IL-4) tip the immunological balance toward a Th1 phenotype for an enhanced antitumor effect. The tetramer assays of antigen-specific CD8⁺ T cells in peripheral blood and spleen demonstrate that mNVs can significantly augment OVA-specific CTLs, accompanied by efficient IFN- γ production. Enhanced CTL infiltration has also

been observed in the tumor area and contributed to antitumor efficacy. Figure 9 schematically depicts the functional pathway of sequential, mNV-triggered antitumor immune processes, including the depot effect, lymph transportation, APC endocytosis and activation, CTL generation, and antitumor efficacy.

Distinctive size effects are observed among extensive characterizations including DC maturation (either *in vitro* or *in vivo*), capacity to generate the antigen-specific CD8⁺ T cells, and tumor prevention and therapy. The advantages of mNV-70 over mNV-150 are likely associated with its virus-mimicking size, which is favorable for an effective immune response. A larger size can be adverse to intracellular dissociation for antigen presentation, as well as timely release of CpG in DC maturation. This was preliminarily supported by a dissociation experiment, in which mNV-150 was found to exhibit an obviously slower disassembly compared with mNV-70 upon DTT treatment.

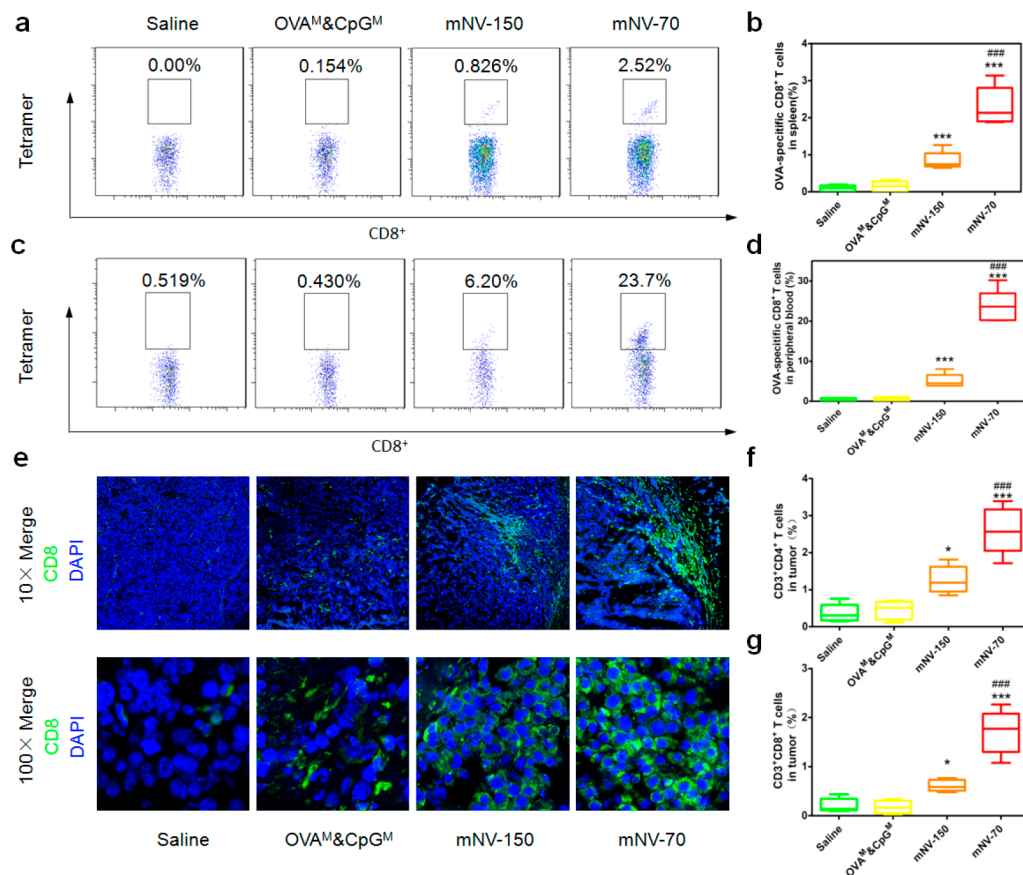


Figure 8. Tetramer assay of OVA-specific CD8⁺ T cells, and tumor-infiltrated CTLs elicited by mNVs in prophylactic test. Shown are their representative scatter plots on day 14 and the frequency of OVA-specific CD8⁺ T cells in (a, b) spleen and (c, d) peripheral blood by flow-cytometry analysis of CD3⁺CD8⁺tetramer⁺ T cells. Tissue cryosections were used to observe CD8⁺ T cell infiltration *in vivo*. (e) Representative immunofluorescence assay of CD8⁺ T cells (green) in B16-OVA melanoma tumors. Two different scales are shown (10× and 100× magnification). The percentages of (f) CD3⁺CD4⁺ T cells and (g) CD3⁺CD8⁺ T cells among total tumor cells were quantitatively determined. Data are presented as mean ± SD (*n* = 5). **p* < 0.05 and ****p* < 0.001 vs the control group; ###*p* < 0.001 vs the mNV-150 group.

CONCLUSION

In summary, a nanovaccine constituted from near whole antigens (97 wt %) has been developed based on an “antigen carries antigen” strategy. The intermolecular disulfide bonds of the antigens were used to cross-link proteins within the nanovaccine, leading to a sulfur network that stabilizes the nanoparticle. Furthermore, the compact, carrier-free, and self-adjuvant nanovaccine, with a high antigen density, significantly promotes a robust T cell immune response and marked LN transportation. This strategy is also highly versatile and potentially universal, as most antigens inherently contain or are conveniently modifiable with cysteine groups.

METHODS

Thermal Assembly of OVA Nanoparticles. Ovalbumin powder was dispersed in 50 mM MES buffer (pH 6.0) at a concentration of 1–10 mg mL⁻¹ and then injected in a screw capped glass test tube. The OVA solution was subject to heat treatment in a water bath at 70 °C and magnetically stirred at 750 rpm thoroughly. The assembly process was closely monitored by opalescence of the reaction, generally accomplished within tens of seconds. At given reaction time, the reaction was terminated by immediately putting the tube in an ice water bath. Finally, the formed nanoparticles were subject to characterization after ultrafiltration.

SDS Assisted Assembly of OVA@CpG Nanoparticles. Thiol-CpG 1826 was first subject to a reduction treatment so as to acquire CpG terminated with free thiol groups (CpG-SH). Ovalbumin

dissolved in DD water (3.0 mg/mL, 1.0 mL) was buffered with 100 mM MES (pH 3.7) at a final concentration of 1.5 mg mL⁻¹ and then injected in a screw capped glass test tube. The solution of SDS (20 μL, 30 mg mL⁻¹) was added, followed by the addition of CpG diluted in diethyl pyrocarbonate (DEPC)-treated water (2 μg μL⁻¹) in different volumes (75, 50, and 37.5 μL for OVA/CpG weight ratios of 20:1, 30:1, and 40:1, respectively). The assembly process was performed in an oil bath at 90 °C under rigorous stirring, with the reaction time from several to tens of minutes. At given reaction time, the reaction was terminated by immediately cooling in an ice water bath. Finally, the formed nanoparticles were subject to characterization after ultrafiltration.

Immunization Protocol for Prophylactic Experiment. The C57BL/6 mice (6–8 weeks old) were randomly divided into five groups (*n* = 10) and immunized as follows: four groups of the mice were subcutaneously injected with 150 μL of saline, mNV-70 (1 mg mL⁻¹), mNV-150 (1 mg mL⁻¹), or molecular formulation (OVA^M&CpG^M, equivalent dosage to nanovaccine), three times at one-week intervals; one group was immunized with complete Freund’s adjuvant (FA) supplemented with equivalent OVA as the control. One week after the final immunization, each mouse was subcutaneously injected with 5 × 10⁴ B16-OVA cells in the right flank, and animals were monitored for tumor growth and body weight. Thereafter, the tumor volume was estimated using the following formula: (short diameter)² × long diameter × 0.5. Tumor growth was measured at 3 day intervals for 24 days.

Evaluation of Lymphocyte Activation and T Cell Response by Flow Cytometry. On day 14, mice were euthanized to collect spleens, draining LNs, tumors, and peripheral blood for immuno-

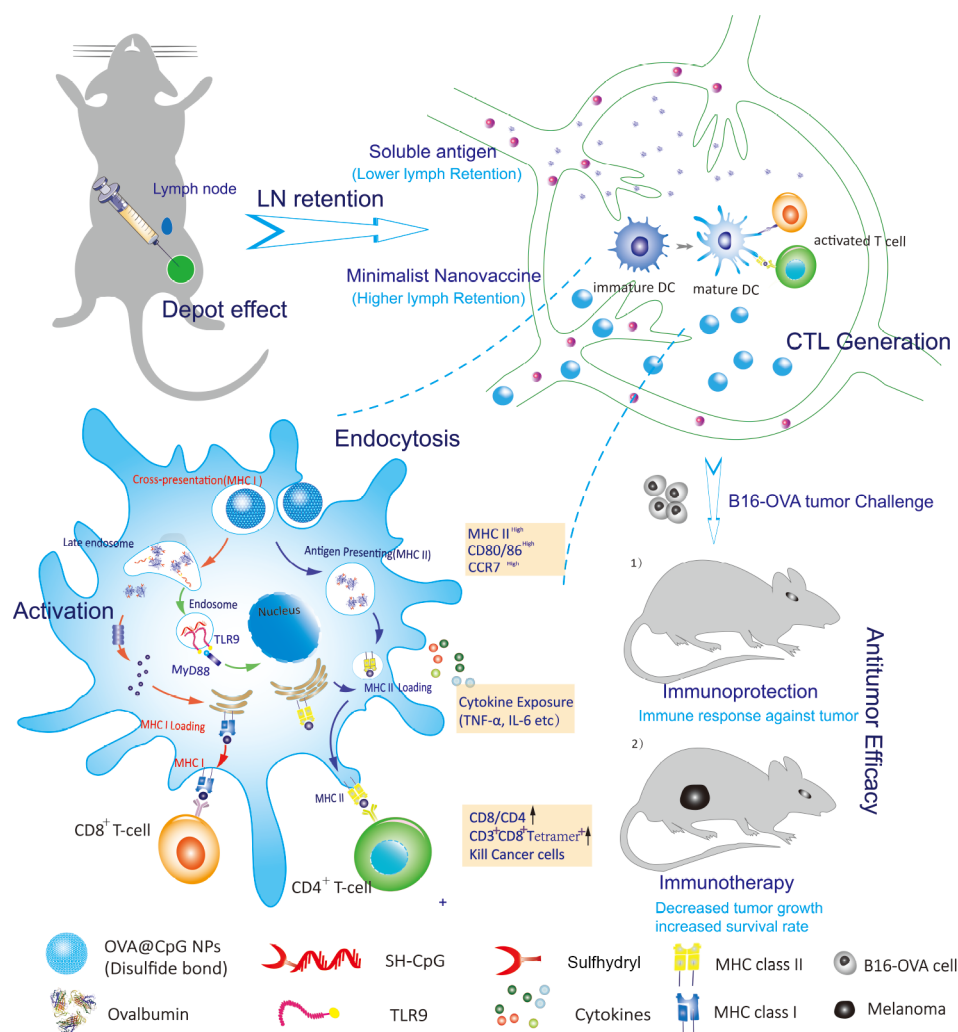


Figure 9. Schematic illustration of mNV-triggered antitumor immune responses. **Depot effect:** mNVs function in antigen protection and sustained release at the site of injection. **Lymph transportation:** mNVs diffuse into LNs as a result of their favorable size (20–200 nm nanoparticles transport and accumulate in LNs). **APC endocytosis:** mNVs significantly promote the cellular uptake efficiency of antigen OVA and CpG by APCs. CpG internalization subsequently activates TLR9 within DCs to augment antigen-specific immunity. **APC activation:** DCs, as the most efficient APCs, are shown here. mNVs with proper size promote DC recognition and interactions. After activation, DCs upregulate costimulatory molecules (CD80, CD86, and CD40), CCR7, and MHC II. **CTL generation:** Activated DCs will subsequently be directed toward LNs, activating antigen-specific T lymphocytes through MHC complexes. **Antitumor efficacy:** The antitumor immunity generated by mNVs elicits potent protection against tumors, suppresses tumor growth, and prolongs the mean survival time.

logical assays. Serum was stored at -80°C and subsequently analyzed by enzyme-linked immunosorbent assay (ELISA).

The isolated tissues (tumor, draining LN, and spleen) were cut into pieces and inflated in digestion solution (2 mg mL^{-1} collagenase IV, 0.1 mg mL^{-1} DNase I in 10% FBS complete medium), followed by incubation for 30 min (60 min for tumor) at 37°C with continuous shaking. The above digested tissues were then gently ground to acquire single-cell suspensions through a $70\text{ }\mu\text{m}$ strainer. For splenic single-cell suspensions, upon completion of digestion, an additional step was applied to lysis red blood cell using $1\times$ RBC lysis buffer. Of special note are treatments of spleen in a bacteria-free operating environment.

The peripheral blood was placed in an anticoagulant tube and centrifuged at 2000 rpm to remove the supernatant. The resulting precipitates were incubated with 3 mL of $1\times$ RBC lysis buffer for 5 min, centrifuged, and washed twice, then repeated lysis 1–2 times to remove the red blood cell thoroughly. The procedures of flow cytometry are shown in [Supporting Information](#).

Immunization for the Established Tumor. To test the therapy effect of mNVs, 5×10^4 B16-OVA cells were subcutaneously injected

in the right flank of animals on day 0. The C57BL/6 mice (6–8 weeks old) were randomly divided into four groups ($n = 6$) and immunized as follows: the mice were subcutaneously injected with $150\text{ }\mu\text{L}$ of saline, mNV-70 (1 mg mL^{-1}), mNV-150 (1 mg mL^{-1}), or molecular formulation (OVA^M&CpG^M, equivalent dosage to nanovaccine), three times on day 4, 8, and 12. Local tumor growth and body weight were evaluated. To assess the effect of mNVs against a larger dose of tumor cells, a ten-fold larger population of B16-OVA cells (5×10^5) were subcutaneously inoculated into C57BL/6 mice ($n = 5$) according to the vaccination protocol described above.

ASSOCIATED CONTENT

Supporting Information

The Supporting Information is available free of charge on the ACS Publications website at DOI: [10.1021/acsnano.8b00558](https://doi.org/10.1021/acsnano.8b00558).

More information on the materials and methods, physicochemical characterization of nanoparticles, gating strategy in flow cytometry, and additional *in vitro* and *in vivo* characterizations of nanovaccine (PDF)

AUTHOR INFORMATION

Corresponding Author

*E-mail: yongyong_li@tongji.edu.cn.

ORCID 

Yongyong Li: 0000-0002-6688-5978

Author Contributions

[#]K.W. and S.W. contributed equally.

Notes

The authors declare no competing financial interest.

ACKNOWLEDGMENTS

This work was financially supported through grants from the National Natural Science Foundation of China (Nos. 51773154, 31771090, 51473124, and 81571801), Shanghai Science and Technology Innovation (Grant 18JC1414500), Shanghai Natural Science Foundation (Grant 17ZR1432100), and Young Hundred-Talent Program of Tongji University.

REFERENCES

- (1) Irvine, D. J.; Swartz, M. A.; Szeto, G. L. Engineering Synthetic Vaccines Using Cues from Natural Immunity. *Nat. Mater.* **2013**, *12*, 978–990.
- (2) Zhao, L.; Seth, A.; Wibowo, N.; Zhao, C. X.; Mitter, N.; Yu, C. Z.; Middelberg, A. P. J. Nanoparticle Vaccines. *Vaccine* **2014**, *32*, 327–337.
- (3) Vartak, A.; Sucheck, S. J. Recent Advances in Subunit Vaccine Carriers. *Vaccines* **2016**, *4*, 12.
- (4) Reed, S. G.; Orr, M. T.; Fox, C. B. Key Roles of Adjuvants in Modern Vaccines. *Nat. Med.* **2013**, *19*, 1597–1608.
- (5) Christensen, D. Vaccine Adjuvants: Why and How. *Hum. Vaccines Immunother.* **2016**, *12*, 2709–2711.
- (6) Li, X. R.; Aldayel, A. M.; Cui, Z. R. Aluminum Hydroxide Nanoparticles Show a Stronger Vaccine Adjuvant Activity than Traditional Aluminum Hydroxide Microparticles. *J. Controlled Release* **2014**, *173*, 148–157.
- (7) Banday, A. H.; Jeelani, S.; Hruby, V. J. Cancer Vaccine Adjuvants - Recent Clinical Progress and Future Perspectives. *Immunopharmacol. Immunotoxicol.* **2015**, *37*, 1–11.
- (8) Hubbell, J. A.; Thomas, S. N.; Swartz, M. A. Materials Engineering for Immunomodulation. *Nature* **2009**, *462*, 449–460.
- (9) Smith, J. D.; Morton, L. D.; Ulery, B. D. Nanoparticles as Synthetic Vaccines. *Curr. Opin. Biotechnol.* **2015**, *34*, 217–224.
- (10) Luo, M.; Wang, H.; Wang, Z.; Cai, H.; Lu, Z.; Li, Y.; Du, M.; Huang, G.; Wang, C.; Chen, X.; et al. A STING-activating Nanovaccine for Cancer immunotherapy. *Nat. Nanotechnol.* **2017**, *12*, 648–654.
- (11) Moon, J. J.; Suh, H.; Bershteyn, A.; Stephan, M. T.; Liu, H. P.; Huang, B.; Sohail, M.; Luo, S.; Ho Um, S.; Khant, H.; Goodwin, J. T.; Ramos, J.; Chiu, W.; Irvine, D. J. Interbilayer-crosslinked Multilamellar Vesicles as Synthetic Vaccines for Potent Humoral and Cellular Immune Responses. *Nat. Mater.* **2011**, *10*, 243–251.
- (12) Chen, Q.; Xu, L. G.; Liang, C.; Wang, C.; Peng, R.; Liu, Z. Photothermal Therapy with Immune-adjuvant Nanoparticles Together with Checkpoint Blockade for Effective Cancer Immunotherapy. *Nat. Commun.* **2016**, *7*, 13193.
- (13) Guo, Y.; Wang, D.; Song, Q.; Wu, T.; Zhuang, X.; Bao, Y.; Kong, M.; Qi, Y.; Tan, S.; Zhang, Z. Erythrocyte Membrane-Enveloped Polymeric Nanoparticles as Nanovaccine for Induction of Antitumor Immunity against Melanoma. *ACS Nano* **2015**, *9*, 6918–6933.
- (14) Kasturi, S. P.; Skountzou, I.; Albrecht, R. A.; Koutsonanos, D.; Hua, T.; Nakaya, H. I.; Ravindran, R.; Stewart, S.; Alam, M.; Kwissa, M.; Villinger, F.; Murthy, N.; Steel, J.; Jacob, J.; Hogan, R. J.; Garcia-Sastre, A.; Compans, R.; Pulendran, B. Programming the Magnitude and Persistence of Antibody Responses with Innate Immunity. *Nature* **2011**, *470*, 543–547.
- (15) Lizotte, P.; Wen, A.; Sheen, M.; Fields, J.; Rojanasopondist, P.; Steinmetz, N.; Fiering, S. In Situ Vaccination with Cowpea Mosaic Virus Nanoparticles Suppresses Metastatic Cancer. *Nat. Nanotechnol.* **2016**, *11*, 295–303.
- (16) Joshi, V. B.; Geary, S. M.; Salem, A. K. Biodegradable Particles as Vaccine Antigen Delivery Systems for Stimulating Cellular Immune Responses. *Hum. Vaccines Immunother.* **2013**, *9*, 2584–2590.
- (17) Ali, O. A.; Huebsch, N.; Cao, L.; Dranoff, G.; Mooney, D. J. Infection-Mimicking Materials to Program Dendritic Cells. *Nat. Mater.* **2009**, *8*, 151–158.
- (18) Irvine, D. J.; Hanson, M. C.; Rakhra, K.; Tokatlian, T. Synthetic Nanoparticles for Vaccines and Immunotherapy. *Chem. Rev.* **2015**, *115*, 11109–11146.
- (19) Wang, Y.; Gu, H. C. Core-Shell-Type Magnetic Mesoporous Silica Nanocomposites for Bioimaging and Therapeutic Agent Delivery. *Adv. Mater.* **2015**, *27*, 576–585.
- (20) Bertrand, N.; Wu, J.; Xu, X. Y.; Kamaly, N.; Farokhzad, O. C. Cancer Nanotechnology: The Impact of Passive and Active Targeting in the Era of Modern Cancer Biology. *Adv. Drug Delivery Rev.* **2014**, *66*, 2–25.
- (21) Gu, Z.; Biswas, A.; Zhao, M. X.; Tang, Y. Tailoring Nanocarriers for Intracellular Protein Delivery. *Chem. Soc. Rev.* **2011**, *40*, 3638–3655.
- (22) Chou, L. Y. T.; Ming, K.; Chan, W. C. W. Strategies for the Intracellular Delivery of Nanoparticles. *Chem. Soc. Rev.* **2011**, *40*, 233–245.
- (23) Nicolas, J.; Mura, S.; Brambilla, D.; Mackiewicz, N.; Couvreur, P. Design, Functionalization Strategies and Biomedical Applications of Targeted Biodegradable/biocompatible Polymer-based Nanocarriers for Drug Delivery. *Chem. Soc. Rev.* **2013**, *42*, 1147–1235.
- (24) Dykman, L.; Khlebtsov, N. Gold Nanoparticles in Biomedical Applications: Recent Advances and Perspectives. *Chem. Soc. Rev.* **2012**, *41*, 2256–2282.
- (25) Chong, C. S.; Cao, M.; Wong, W. W.; Fischer, K. P.; Addison, W. R.; Kwon, G. S.; Tyrrell, D. L.; Samuel, J. Enhancement of T Helper Type 1 Immune Responses against Hepatitis B virus Core Antigen by PLGA Nanoparticle Vaccine Delivery. *J. Controlled Release* **2005**, *102*, 85–99.
- (26) Mamo, T.; Poland, G. A. Nanovaccinology: The Next Generation of Vaccines Meets 21st Century Materials Science and Engineering. *Vaccine* **2012**, *30*, 6609–6611.
- (27) Henry, C. E.; Wang, Y. Y.; Yang, Q.; Hoang, T.; Chattopadhyay, S.; Hoen, T.; Ensign, L. M.; Nunn, K. L.; Schroeder, H.; McCallen, J.; Moench, T.; Cone, R.; Roffler, S. R.; Lai, S. K. Anti-PEG Antibodies Alter the Mobility and Biodistribution of Densely PEGylated Nanoparticles in Mucus. *Acta Biomater.* **2016**, *43*, 61–70.
- (28) Shiraishi, K.; Kawano, K.; Maitani, Y.; Aoshi, T.; Ishii, K. J.; Sanada, Y.; Mochizuki, S.; Sakurai, K.; Yokoyama, M. Exploring the Relationship Between Anti-PEG IgM Behaviors and PEGylated Nanoparticles and Its Significance for Accelerated Blood Clearance. *J. Controlled Release* **2016**, *234*, 59–67.
- (29) Riaz, N.; Havel, J. J.; Kendall, S. M.; Makarov, V.; Walsh, L. A.; Desrichard, A.; Weinhold, N.; Chan, T. A. Recurrent SERPINB3 and SERPINB4 Mutations in Patients Who Respond to Anti-CTLA4 Immunotherapy. *Nat. Genet.* **2016**, *48*, 1327–1329.
- (30) Bode, C.; Zhao, G.; Steinhagen, F.; Kinjo, T.; Klinman, D. M. CpG DNA as a Vaccine Adjuvant. *Expert Rev. Vaccines* **2011**, *10*, 499–511.
- (31) Kuai, R.; Ochyl, L. J.; Bahjat, K. S.; Schwendeman, A.; Moon, J. J. Designer Vaccine Nanodiscs for Personalized Cancer Immunotherapy. *Nat. Mater.* **2017**, *16*, 489–496.
- (32) Ma, Q.; Zhou, D. P.; DeLyria, E. S.; Wen, X. X.; Lu, W.; Thapa, P.; Liu, C. W.; Li, D.; Bassett, R. L.; Overwijk, W. W.; Hwu, P.; Li, C. Synthetic Poly(L-Glutamic Acid)-conjugated CpG Exhibits Antitumor Efficacy with Increased Retention in Tumor and Draining Lymph Nodes after Intratumoral Injection in a Mouse Model of Melanoma. *J. Immunother.* **2017**, *40*, 11–20.

- (33) Guo, Y. Y.; Wang, D.; Song, Q. L.; Wu, T. T.; Zhuang, X. T.; Bao, Y. L.; Kong, M.; Qi, Y.; Tan, S. W.; Zhang, Z. P. Erythrocyte Membrane-Enveloped Polymeric Nanoparticles as Nanovaccine for Induction of Antitumor Immunity against Melanoma. *ACS Nano* **2015**, *9*, 6918–6933.
- (34) Huntington, J. A.; Stein, P. E. Structure and Properties of Ovalbumin. *J. Chromatogr., Biomed. Appl.* **2001**, *756*, 189–198.
- (35) Wei, H.; Zhuo, R. X.; Zhang, X. Z. Design and Development of Polymeric Micelles with Cleavable Links for Intracellular Drug Delivery. *Prog. Polym. Sci.* **2013**, *38*, 503–535.
- (36) Leifer, C. A.; Kennedy, M. N.; Mazzoni, A.; Lee, C.; Kruhlak, M. J.; Segal, D. M. TLR9 is Localized in the Endoplasmic Reticulum Prior to Stimulation. *J. Immunol.* **2004**, *173*, 1179–1183.
- (37) Li-Chan, E. C.; Powrie, W. D.; Nakai, S. The Chemistry of Eggs and Egg Products. *Egg science and technology* **1995**, *4*, 105–75.
- (38) Ruan, Q. J.; Chen, Y. M.; Kong, X. Z.; Hua, Y. F. Heat-induced Aggregation and Sulphydryl/disulphide Reaction Products of Soy Protein with Different Sulphydryl Contents. *Food Chem.* **2014**, *156*, 14–22.
- (39) Banchereau, J.; Steinman, R. Dendritic Cells and the Control of Immunity. *Nature* **1998**, *392*, 245–52.
- (40) Paulis, L. E.; Mandal, S.; Kreutz, M.; Figdor, C. G. Dendritic Cell-based Nanovaccines for Cancer Immunotherapy. *Curr. Opin. Immunol.* **2013**, *25*, 389–395.
- (41) Forster, R.; Davalos-Miszlitz, A. C.; Rot, A. CCR7 and Its Ligands: Balancing Immunity and Tolerance. *Nat. Rev. Immunol.* **2008**, *8*, 362–371.
- (42) Li, A.; Qin, L. L.; Wang, W. R.; Zhu, R. R.; Yu, Y. C.; Liu, H.; Wang, S. L. The Use of Layered Double Hydroxides as DNA Vaccine Delivery Vector for Enhancement of Anti-melanoma Immune Response. *Biomaterials* **2011**, *32*, 469–477.
- (43) Kourtis, I. C.; Hirose, S.; de Titta, A.; Kontos, S.; Stegmann, T.; Hubbell, J. A.; Swartz, M. A. Peripherally Administered Nanoparticles Target Monocytic Myeloid Cells, Secondary Lymphoid Organs and Tumors in Mice. *PLoS One* **2013**, *8*, No. e61646.
- (44) Morsy, M. A.; Norman, P. J.; Mitry, R.; Rela, M.; Heaton, N. D.; Vaughan, R. W. Isolation, Purification and Flow Cytometric Analysis of Human Intrahepatic Lymphocytes Using an Improved Technique. *Lab. Invest.* **2005**, *85*, 285–296.
- (45) Yu, Y. R. A.; O'Koren, E. G.; Hotten, D. F.; Kan, M. J.; Kopin, D.; Nelson, E. R.; Que, L.; Gunn, M. D. A Protocol for the Comprehensive Flow Cytometric Analysis of Immune Cells in Normal and Inflamed Murine Non-lymphoid Tissues. *PLoS One* **2016**, *11*, No. e0150606.
- (46) Shindo, G.; Endo, T.; Onda, M.; Goto, S.; Miyamoto, Y.; Kaneko, T. Is the CD4/CD8 Ratio an Effective Indicator for Clinical Estimation of Adoptive Immunotherapy for Cancer Treatment? *J. Cancer Ther.* **2013**, *4*, 1382–1390.
- (47) Apte, S. H.; Groves, P.; Olver, S.; Baz, A.; Doolan, D. L.; Kelso, A.; Kienzle, N. IFN-gamma Inhibits IL-4-Induced Type 2 Cytokine Expression by CD8 T Cells *In Vivo* and Modulates the Anti-Tumor Response. *J. Immunol.* **2010**, *185*, 998–1004.